# Gas-liquid heat transfer in a bubble collapsing near a wall

H. Yuan and A. Prosperetti
*Department of Mechanical Engineering, The Johns Hopkins University, Baltimore, Maryland 21218*

(Received 26 April 1996; accepted 16 September 1996)

The collapse of a gas bubble near a solid wall is studied numerically by assuming the liquid to be incompressible and the Mach number of the gas flow to be small. The liquid motion is simulated by a boundary integral method and the gas thermo-fluid dynamics by finite differences on a boundary-fitted grid. With the physical properties of a liquid monopropellant, it is found that the liquid heating is essentially localized in the microjet, but is probably not sufficient to cause spontaneous ignition. The reasons for this conclusion — that, while being in general agreement with available experimental evidence, is at variance with deductions from previous spherical collapse calculations — are elucidated. © *1997 American Institute of Physics.* [S1070-6631(97)01101-X]

## I. INTRODUCTION

The increasing technological importance of liquid monopropellants such as LGP 1845 and 1846 motivates a strong interest in the safe operational limits of their use. Occasionally, unexplained ignitions have occurred upon strong impacts.[1] One of the mechanisms suggested to explain these occurrences is heating of the liquid due to the compression of entrained gas bubbles.[2] Indeed it is well known that, due to the kinetic energy accumulated in the liquid, a bubble can be readily compressed to a small fraction of its initial volume. By assuming adiabatic heating, the absolute temperature of an air bubble would increase by nearly 16 times for a radius reduction of 1 order of magnitude. Since current estimates suggest that ignition requires ''hot spots'' with typical dimensions of 0.1 to 10 $\mu$m, durations of 10 to 1000 $\mu$s, and temperatures in excess of 700 K,[2] it would seem that ignition could readily be achieved in this way if the liquid in contact with the bubble is heated to comparable temperatures. Experiments designed to study the process, however, have failed to provide an unambiguous confirmation of this hypothesis.[3,4] Although there is evidence of reaction in the gas phase, achieving ignition of the liquid has been found much harder than expected.

An important aspect of the previous argument is, of course, the heat transport from the gas to the liquid. To examine this point, we have performed calculations with the spherical collapse model of Refs. 5 and 6 (which includes a correction for liquid compressibility). With overpressures between 10 and 300 atm, we have found that the liquid heating during the first collapse is sharply lower than the estimated adiabatic temperatures. However, after the sudden application of an overpressure, the first collapse is followed by a series of damped oscillations (see, e.g., Figs. 3 to 5 below) in the course of which the liquid heats up further to the point where ignition should have occurred in the conditions of the experiments mentioned earlier.

In this paper we refine our earlier spherical calculations by allowing for the deformation of the bubble. Due to buoyancy, bubbles are expected to be frequently found near solid boundaries, which are well-known to induce the formation of jets in the course of the collapse (see, e.g., Refs. 7–11). Upon strong compression, one expects the jet to be sufficiently energetic to pierce the bubble and lead to its fragmentation. Thus, unless the jet itself heats up sufficiently, the liquid would not reach ignition conditions.

For this reason, contrary to all previous analyses with the exception of a recent paper by Takahira *et al.*,[12] we not only allow for the deformation, but also study the temperature field inside and outside the bubble and in particular in the jet. By adopting a different route than that of Ref. 12 for the solution of the thermofluid problem in the gas, we are able to achieve a much greater resolution of the thermal boundary layer.

For simplicity, we assume an axisymmetric geometry. The liquid motion is treated as incompressible and inviscid. The gas is assumed to be perfect and its pressure spatially uniform. To account for the time dependence of the computational domain, we use a boundary integral method for the liquid and a boundary-fitted grid for the bubble interior.

## II. MATHEMATICAL MODEL

We consider a bubble in a semi-infinite expanse of liquid bounded by a rigid plane wall under the assumption of axial symmetry. What differentiates the present study from earlier ones dealing with a similar geometry is the manner in which the bubble internal pressure $p$ is calculated. Earlier studies assumed either a constant value, which is appropriate for a bubble containing only relatively low-density vapor, or a polytropic relation $p \propto 1/V^{\kappa}$, where $V$ is the instantaneous bubble volume and $\kappa$ a polytropic index. We propose instead to calculate the internal pressure accounting for the nonuniformity of the temperature distribution extending the approach of Refs. 13 and 14. The major difficulty is of course the fact that the computational domain varies with time.

### A. Liquid

Since the liquids of present concern are only slightly viscous and the flow we consider is highly transient, we disregard viscous effects and assume the flow to be irrotational, $\mathbf{v}=\nabla\phi$. As will be seen later, flow velocities are far smaller than the speed of sound in the liquid except possibly in the very last instants of the collapse, which enables us to assume the liquid to be incompressible:

$$\nabla^2\phi=0. \tag{1}$$

By using Green's identity, the formal solution of the Laplace equation (1) can be expressed as a boundary integral. With the assumption of axial symmetry, the angular integration can be carried out explicitly in the usual way to find[15–18]

$$\phi(\mathbf{x}) = \int_S \left[ G(\mathbf{x},\mathbf{x}_s)\frac{\partial \phi(\mathbf{x}_s)}{\partial n_s} - H(\mathbf{x},\mathbf{x}_s)\phi(\mathbf{x}_s) \right] dS, \tag{2}$$

where the integral is over the trace of the bubble surface on a meridian plane and its image in the neighboring plane boundary, $\partial/\partial n_s$ is the derivative in the normal direction oriented away from the liquid, and

$$\begin{aligned} G(\mathbf{x},\mathbf{x}_s) &= G(R,Z;r,z) = \frac{2r}{\pi}\frac{K(m)}{A^{1/2}}, \\ H(\mathbf{x},\mathbf{x}_s) &= H(R,Z;r,z) = \frac{2r}{\pi}\frac{\partial}{\partial n}\frac{K(m)}{A^{1/2}}, \end{aligned} \tag{3}$$

with $K(m)$ the complete elliptic integral of the first kind and

$$A = (R+r)^2 + (Z-z)^2, \quad m = \frac{4rR}{A}. \tag{4}$$

In these expressions $\mathbf{x}=(R,Z)$ is the position of the field point in the azimuthal plane expressed in cylindrical coordinates and $\mathbf{x}_s=(r,z)$ is the position of the source point.

The value of $\phi$ at the bubble surface is found by integrating in time the Bernoulli integral evaluated at the surface

$$\frac{\partial \phi}{\partial t} + \frac{1}{2}|\nabla \phi|^2 = \frac{p_\infty - p + \sigma \mathscr{C}}{\rho_L}. \tag{5}$$

Here, $p$ is the pressure in the bubble, $p_\infty$ the ambient pressure, $\sigma$ the surface tension coefficient, and $\mathscr{C}$ the local surface curvature. The processes we simulate are too rapid and occur on a scale too small to be significantly affected by gravity which, accordingly, has been disregarded. The velocity normal to the surface, $\partial\phi/\partial n_s$, is found by solving (2) once the surface value of $\phi$ has been updated. A knowledge of the normal velocity permits then the new surface position to be determined by integrating in time the kinematic boundary condition

$$\mathbf{n}\cdot\frac{d\mathbf{x}}{dt} = \mathbf{n}\cdot\nabla\phi. \tag{6}$$

Since the bubble surface is a purely geometrical entity, only its normal velocity $v_\perp = \mathbf{n}\cdot\nabla\phi$ is physically meaningful. The tangential component $V_\parallel$ can be chosen arbitrarily, and this freedom will be used in the next section for numerical convenience. Upon using (5) to express $\partial\phi/\partial t$, the convective derivative of the potential following the surface becomes

$$\begin{aligned} \frac{d\phi}{dt} \equiv \frac{\partial\phi}{\partial t} + v_\perp\frac{\partial\phi}{\partial n} + V_\parallel\frac{\partial\phi}{\partial s} &= \frac{p_\infty - p + \sigma\mathscr{C}}{\rho_L} + \frac{1}{2}v_\perp^2 \\ &\quad + v_\parallel\left(V_\parallel - \tfrac{1}{2}v_\parallel\right), \end{aligned} \tag{7}$$

where $v_\parallel \equiv \partial\phi/\partial s$, the derivative of the potential with respect to the arc length $s$ along the surface.

As the bubble collapses, the gas undergoes a very significant heating that also affects the liquid temperature in the neighborhood of the free surface. However, it is easy to show (see, e.g., Ref. 6) that, due to the short times involved and the huge differences between the volumic heat capacities of the two phases, the temperature drop between the bubble core and the liquid surface is much greater than between the surface and the ambient liquid. Therefore, in the interest of simplicity, we shall not consider the energy equation in the liquid. The liquid temperature rise will be estimated approximately after the heat transfer rate across the bubble boundary has been obtained.

### B. Gas

A considerable simplification of the mathematical problem in the bubble can be achieved by recognizing that the maximum pressure difference $\Delta p$ between two points is of the order

$$\frac{\Delta p}{p} \sim \frac{U^2}{c^2}, \tag{8}$$

where $c$ is the speed of sound in the gas.[14,19] The characteristic collapse velocity $U$ is of the order of $\sqrt{(p_\infty - p)/\rho_L}$ (see, e.g., Ref. 20), and therefore much smaller than $c$. This estimate (8) enables us to neglect the spatial dependence of $p$ in the bubble thus replacing the gas momentum equation by the simple statement

$$p \simeq p(t). \tag{9}$$

An analysis of this approximation for the spherical case was carried out in Ref. 19 where it was found to be very good.

The estimate (8) assumes that no discontinuities arise in the gas. On the basis of an approximate analysis, Greenspan and Nadim[21] estimate that the time $t_S$ of shock formation for a spherical surface at rest at the initial time, but possessing an inward (negative) acceleration $\ddot{a}_0$, is

$$t_S \simeq \frac{a_0}{c_0}\left\{1 - \exp\left[\frac{2c_0^2}{(\gamma+1)a_0\ddot{a}_0}\right]\right\}, \tag{10}$$

where $a_0$ is the inital radius and $c_0$ the speed of sound in the initial state. For a spherical cavity subject to an initial overpressure $\Delta P$, from the Rayleigh–Plesset equation, we may estimate that $a_0\ddot{a}_0 \simeq \Delta p/\rho$. With the values used in the numerical examples given later, we find that the argument of the exponential has a value of the order of $-30$. This fact implies that $t_S \simeq a_0/c_0$, i.e., that pressure perturbations in the gas tend to remain acoustic. Phenomena such as shock heating are therefore ruled out.

At liquid temperatures cold enough that the vapor pressure is small compared with $p_\infty$, the bubble contents can be approximated as entirely consisting of an incondensable gas. We shall further assume that the gas has constant specific heats and obeys the perfect gas law

$$p = \mathscr{R}\rho_G T, \tag{11}$$

where $\mathscr{R}$ is the universal gas constant divided by the molecular mass, $\rho_G$ is the density, and $T$ is the temperature. With these assumptions, by combining the energy and continuity equations, we find

$$\nabla\cdot[(\gamma-1)k\nabla T+\gamma p\mathbf{u}]=\dot{p}, \tag{12}$$

where $k$ is the gas thermal conductivity, $\gamma$ the ratio of specific heats, and $\dot{p}\equiv dp/dt$. In view of (9), this equation can be integrated to find

$$(\gamma-1)k\nabla T+\gamma p\mathbf{u}=\tfrac{1}{3}\dot{p}\mathbf{x}+\nabla\times\mathbf{B}, \tag{13}$$

where $\mathbf{x}$ is the position vector and the field $\mathbf{B}$ is to be determined. Upon taking the curl of this relation to calculate the vorticity, since $k$ depends on $T$ and $p$, we find

$$\nabla\times\mathbf{u}=\frac{1}{\gamma p}\nabla\times\nabla\times\mathbf{B}. \tag{14}$$

Vorticity can only be generated at the bubble surface from which, in the flow considered here, it does not have much time to diffuse into the bubble core. Convective transport in the normal direction is also negligible during the collapse phase because, near the bubble wall, the relative normal velocity is into the wall. This argument justifies assuming that $\nabla\times\mathbf{u}\simeq 0$ from which we find $\nabla\times\nabla\times\mathbf{B}=0$ or $\nabla\times\mathbf{B}=\nabla\Phi$ with

$$\nabla^2\Phi=0. \tag{15}$$

We can thus write the gas velocity field in the form

$$\mathbf{u}=\frac{1}{\gamma p}\left[\frac{1}{3}\dot{p}\mathbf{x}-(\gamma-1)k\nabla T+\nabla\Phi\right]. \tag{16}$$

On the basis of (15) it can be said that, in a sense, the potential $\Phi$ carries the ''incompressible'' part of the velocity field. Takahira *et al.*[12] wrote the entire right-hand side of (16) as the gradient of a potential, which therefore satisfies a Poisson, rather than the Laplace, equation. In solving this equation by a boundary integral method, they then had to carry also a computationally expensive volume integral.

One of the key points of this work is the analysis of the temperature distribution in the gas, which requires a consideration of the energy equation in a form different from (12)

$$\rho_G C_p\frac{dT}{dt}=\nabla\cdot(k\nabla T)+\dot{p}, \tag{17}$$

where $C_p$ is the (constant) specific heat at constant pressure and $d/dt$ is the convective derivative. As explained in the next section, we solve the problem on a moving grid. For this reason, we write the convective derivative in the form

$$\frac{dT}{dt}=\left(\frac{\partial T}{\partial t}\right)_{\text{node}}+(\mathbf{u}-\mathbf{V})\cdot\nabla T, \tag{18}$$

in which the gas velocity $\mathbf{u}$ is given by (16) and $\mathbf{V}$ is the grid velocity to be specified later. The subscript ''node'' signifies that the partial time derivative is taken following the motion of a node on the moving grid.

Since the energy equation in the form (12) follows from (17) and continuity, the simultaneous use of (12) and (17) is equivalent to enforcing conservation of both energy and mass.

In view of the strong temperature changes in the bubble, it is desirable to account for the temperature dependence of the thermal conductivity $k$. Following Ref. 14, we use the linear relation

$$k=AT+B, \tag{19}$$

with the constants $A$ and $B$ chosen to approximate the measured values over a suitable temperature range. For air, over the temperature range 200 to 3000 K, we use $A = 5.28\times 10^{-5}\,\mathrm{W/m\,K^2}$, $B = 1.165\times 10^{-2}\,\mathrm{W/m\,K}$.[14]

### C. Boundary conditions

At the bubble boundary the normal gas velocity must equal that of the liquid so that

$$\frac{1}{\gamma p}[\tfrac{1}{3}\dot{p}\mathbf{x}-(\gamma-1)k\nabla T+\nabla\Phi]\cdot\mathbf{n}=\nabla\phi\cdot\mathbf{n}. \tag{20}$$

In the solution procedure described in the next section, this relation takes on the role of a Neumann condition on $\Phi$.

Upon integrating the gas energy equation in the form (12) over the bubble volume, we find the following equation for the gas pressure:

$$\dot{p}=-\gamma p\frac{\dot{V}}{V}-\frac{\gamma-1}{V}Q, \tag{21}$$

where $V$ is the instantaneous bubble volume and the total heat $Q$ crossing the bubble boundary per unit time from the gas into the liquid (i.e., in the direction opposite to that of the normal $\mathbf{n}$) is given by

$$Q=\int_S k\nabla T\cdot\mathbf{n}\,dS. \tag{22}$$

The rate of change of the bubble volume is given by

$$\dot{V}=\int_S\mathbf{u}\cdot\mathbf{n}\,dS. \tag{23}$$

It may be noted that, if $Q = 0$ (or $\gamma = 1$), Eq. (21) shows the gas pressure to satisfy the adiabatic relation as in most of the earlier models mentioned before. The essence of the present work lies therefore in the calculation of $Q$.

In principle, the boundary conditions on the temperature are the continuity of temperature and (if phase change is disregarded) heat flux at the bubble surface. As noted before, and as discussed quantitatively in Ref. 6, for the purpose of calculating the gas temperature the liquid heating can be neglected so that

$$T=T_\infty, \tag{24}$$

where $T_\infty$ is the undisturbed liquid temperature. With this condition, the surface heat flux is determined.

## III. NUMERICAL METHOD

The mathematical formulation described in the previous section consists of a set of highly coupled equations. An implicit solution method fully reflexive of this coupling would of course be desirable, but also computationally demanding. For this reason we advance the solution in the liq-

uid explicitly using the current value of the pressure in the gas, and limit the use of implicit coupling to the gas problem.

### A. Liquid

The time step is initiated by calculating the velocity potential on the bubble surface at the next time $t^{n+1}$ by integrating Eq. (7) at each surface node with the third-order Adams-Bashforth algorithm

$$\phi^{n+1}=\phi^n+\frac{\Delta t}{12}\left[23\left(\frac{d\phi}{dt}\right)^n-16\left(\frac{d\phi}{dt}\right)^{n-1}+5\left(\frac{d\phi}{dt}\right)^{n-2}\right], \tag{25}$$

where $d\phi/dt$ is given by (7).

The bubble surface is updated next by integrating (6) along the normal direction. The accuracy of this step and the stability of the calculation are strongly influenced by errors in the estimation of the normal. For this reason we use a third-order Adams–Bashforth method for the velocity, but an implicit discretization for the normal

$$r^{n+1}=r^n+\frac{n_r^n+n_r^{n+1}}{2}\,\frac{23v_\perp^n-16v_\perp^{n-1}+5v_\perp^{n-2}}{12}\Delta t, \tag{26}$$

$$z^{n+1}=z^n+\frac{n_z^n+n_z^{n+1}}{2}\,\frac{23v_\perp^n-16v_\perp^{n-1}+5v_\perp^{n-2}}{12}\Delta t. \tag{27}$$

These equations are solved iteratively. A cubic spline representation is used for the surface nodes at each iteration and the normal is calculated by analytic differentiation of this representation. In order to prevent the nodes from growing too close or too distant from each other, after convergence, they are displaced along the surface with the aid of the last spline representation so as to become equidistant. This step is equivalent to a specification of the parallel velocity $V_\parallel$ of the interface referred to earlier in connection with Eq. (7).

From the knowledge of the new bubble surface and of the surface potential the tangential velocity $v_\parallel$ can be calculated. For the two nodes on the axis of symmetry we set $v_\parallel = 0$. For any other node $i$ we use centered differences

$$v_\parallel^n=\frac{\phi_{i+1}^n-\phi_{i-1}^n}{\Delta s_\eta}, \tag{28}$$

where $\Delta s_\eta$ is the distance between the two nodes $i\pm1$ approximated by

$$\Delta s_\eta=h_\eta\Delta\eta, \tag{29}$$

where $h_\eta$ the metric coefficient defined below in (47).

To calculate the normal velocity component we use the boundary integral relation (2) much in the same way as in the method described in Ref. 22. A distinctive modification introduced in this work is motivated by the fact that, due to the decreasing area of the surface elements near the poles, the algebraic system is not very well conditioned. To circumvent this problem, on the bubble surface we take as our unknown not $\partial\phi/\partial n\equiv\psi$ but

$$w=r\frac{\partial\phi}{\partial n}=r\psi. \tag{30}$$

The surface, $\phi$, and $w$ are then approximated by cubic splines and the necessary integrations performed by using 8th-order Gauss–Legendre quadrature to form a linear system for $w$

$$\mathbf{Gw}=(\mathbf{I}-\mathbf{H})\boldsymbol{\phi}, \tag{31}$$

where $\mathbf{G}$, $\mathbf{H}$ are square matrices and $\mathbf{w}$, $\boldsymbol{\phi}$ column vectors representing the discretized values of $w$ and $\phi$ at the nodes. The details of the formation of the matrices are described in Ref. 22 and need not be repeated here.

While use of the auxiliary variable $w$ removes the quasi-singularity near the axis of symmetry and gives a natural homogeneous boundary condition at $r=0$, $\partial\phi/\partial n$ still needs to be calculated from $w$. Simply dividing by $r$ would of course essentially re-introduce the error amplification avoided by using $w$. Therefore we use the following spectrum-smoothing inversion procedure. Along the bubble surface we expand $r$, $w$ in sine and $\psi(\eta)=\partial\phi/\partial n$ in cosine series in the dimensionless variable $\eta$ ranging between $-1$ and 1 along the bubble surface. The problem to be solved is then to find $\psi$ given $r(\eta)$ and $w(\eta)$

$$r(\eta)\psi(\eta)=w(\eta). \tag{32}$$

The discrete Fourier transform of this equation is

$$\hat{r}(k)*\hat{\psi}(k)=\hat{w}(k), \tag{33}$$

where $*$ stands for the discrete convolution product. This relation is equivalent to the linear system

$$\mathbf{R}\boldsymbol{\psi}=\mathbf{w}, \tag{34}$$

with $\boldsymbol{\psi}$ and $\mathbf{w}$ column vectors and $\mathbf{R}$ a circulant matrix.[23] We now replace $\mathbf{w}$ by a smoothed low-pass-filtered vector $\mathbf{Fw}$, after which the system (34) is solved by $LU$ decomposition. Typical windows $\mathbf{F}$ are rectangle, Gaussian, Hamming or Hann (see, e.g., Refs. 24 and 25). We have obtained good results using Hann's (sometimes also called raised cosine) form

$$F_k=\frac{1}{2}\left(1+\cos\,\pi\frac{k}{K}\right), \tag{35}$$

where $k$ is the index of the Fourier component and $K$ is a cut-off index above which $F_k = 0$. Ordinarily we take $K$ equal to one half the number of surface nodes.

### B. Gas

When a bubble in equilibrium is set into inward motion by an applied external pressure, the gas temperature field in the core starts increasing uniformly due to adiabatic compression. At the bubble surface, this tendency is in conflict with the boundary condition (24) which requires the temperature to remain undisturbed. A boundary layer structure therefore develops that gradually builds inward from the surface. For sufficiently short times, it is therefore sufficient to solve the gas thermal problem in this boundary layer.

Unlike the work of Takahira *et al.*,[12] we use this observation to avoid the solution of the problem in the full domain of the bubble interior, with a considerable simplification of the grid-generation step.

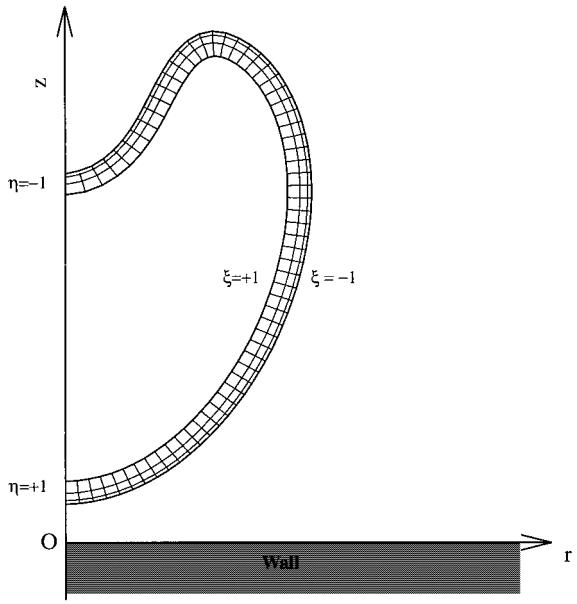


FIG. 1. The boundary-fitted coordinate system. The line $\xi=-1$ is the bubble surface and the line $\xi=1$ the artificial inner boundary. The ''north'' and ''south poles'' correspond to $\eta=-1$ and $+1$ respectively.

### 1. Grid generation

A boundary fitted orthogonal grid is generated in the bubble every time the surface is updated. Since it is only the thermal boundary layer that needs to be discretized, the grid's boundary with the bubble core need not be prescribed and it is therefore possible to use a method based on a hyperbolic, rather than elliptic, formulation. The advantage is a good adaptive control of grid size and the numerical efficiency deriving from the use of a marching algorithm. The procedure is explained in detail in Ref. 26. Here, we describe the general idea concentrating on the grid control method.

An orthogonal mapping transforms the physical domain in the $(r,z)$ plane into the rectangle (right cylinder) $-1\leqslant\xi,\eta\leqslant 1$ in the computational plane

$$r=r(\xi,\eta), \quad z=z(\xi,\eta). \tag{36}$$

Orthogonality is expressed by

$$g_{12}\equiv r_\xi r_\eta+z_\xi z_\eta=0, \tag{37}$$

where the subscripts indicate partial differentiation. The Jacobian $J$ of the transformation

$$r_\xi z_\eta-r_\eta z_\xi=J, \tag{38}$$

multiplied by the differentials $d\xi\, d\eta$, has the geometrical meaning of the area of the surface element of the physical plane mapped into the rectangle $d\xi\, d\eta$ of the computational plane. By prescribing $J$, Eqs. (37) and (38) can therefore be integrated to generate an orthogonal grid with controlled grid spacing.

In the present application we identify the line $\xi=-1$ with the bubble surface and integrate inward to $\xi=1$. The points of the symmetry axis far from, and near, the rigid boundary correspond to $\eta=-1$ and $\eta=1$, respectively (Fig. 1). We use a total of $N_\xi+1$ and $N_\eta+1$ nodes in the $\xi$ and $\eta$ directions, respectively. In the computational plane the nodes are equispaced with $\Delta\xi=2/N_\xi$, $\Delta\eta=2/N_\eta$. In order to transform the uniformly spaced $\xi=$const lines of the computational plane into non-uniformly spaced lines in the physical plane, where a denser grid near the bubble surface is desirable, we prescribe that the distance $\Delta s_\xi$ between two successive lines be given by

$$\Delta s_\xi^n=\tfrac{1}{2}[s(\xi_{n+1})-s(\xi_{n-1})], \tag{39}$$

where $s(\xi)$ is the arc length along the $\eta=$const coordinate lines specified by

$$s(\xi)=L\frac{\tan[\tfrac{1}{4}\epsilon\pi(1+\xi)]}{\tan\tfrac{1}{2}\epsilon\pi}, \tag{40}$$

with $\epsilon\sim 0.5$–$0.8$ and $L$ the total thickness of the grid normal to the bubble surface. At the beginning we typically take $L$ equal to five times the thermal diffusion length $\sqrt{Dt_c}$ based on the thermal diffusivity of the gas $D$ and a characteristic time $t_c$. For the collapse case $t_c$ is taken as the Rayleigh collapse time $t_R$

$$t_R=0.915a\sqrt{\rho_L/\Delta P}, \tag{41}$$

with $a$ the initial bubble radius and $\Delta P$ a characteristic pressure difference. Toward the end of the collapse $L$ is somewhat reduced to prevent the grids from opposite sides of the bubble crossing the surface.

Integration of the system (37), (38) proceeds along the ''time-like'' direction $\xi$. Suppose that the $n$-th coordinate line, $\xi=\xi_n$, has been generated. To generate the $(n+1)$-st, we linearize locally the set of non-linear partial differential equations around $\xi_n$ by writing

$$r_\xi r_\eta^n+r_\xi^n r_\eta+z_\xi^n z_\eta+z_\xi z_\eta^n=0, \tag{42}$$

$$\tfrac{1}{2}(r_\xi z_\eta^n+r_\xi^n z_\eta)-\tfrac{1}{2}(r_\eta z_\xi^n+r_\eta^n z_\xi)=J, \tag{43}$$

where the superscript $n$ indicates values for $\xi=\xi_n$. More compactly, we write this system as

$$\mathbf{W}_\xi+\mathbf{C}\mathbf{W}_\eta=\mathbf{J}, \tag{44}$$

where

$$\mathbf{W}=(r,z)^T, \quad \mathbf{J}=\frac{2J}{(h_\eta^n)^2}(z_\eta^n,-r_\eta^n)^T, \tag{45}$$

and

$$\mathbf{C}=\frac{1}{(h_\eta^n)^2}\begin{bmatrix} r_\xi^n r_\eta^n-z_\xi^n z_\eta^n & r_\xi^n z_\eta^n+r_\eta^n z_\xi^n \\ r_\xi^n z_\eta^n+r_\eta^n z_\xi^n & -r_\xi^n r_\eta^n+z_\xi^n z_\eta^n \end{bmatrix}. \tag{46}$$

The metric coefficient in the $\eta$ direction, $h_\eta$, is given by

$$h_\eta=(r_\eta^2+z_\eta^2)^{1/2}. \tag{47}$$

The derivatives $r_\eta^n$, $z_\eta^n$ appearing in (45), (46), and (47) are calculated analytically by fitting a cubic spline along the coordinate line $\xi_n$. The derivatives in the $\xi$ direction, however, are unknown and this circumstance requires the use of a predictor-corrector method for the integration of (42), (43).

For the predictor step, $r_\xi^n$, $z_\xi^n$ are estimated assuming that each node of the new $\xi=\xi_{n+1}$ line lies along the normal issuing from the corresponding node of the $\xi=\xi_n$ line so that

$$r_\xi^n = \frac{z_\eta^n}{h_\eta}\Delta s_\xi^n, \quad z_\xi^n = -\frac{r_\eta^n}{h_\eta}\Delta s_\xi^n. \tag{48}$$

In the neighborhood of the node $(\xi_n, \eta_i)$, the Jacobian $J_i^n$ is prescribed by writing

$$J_i^n = \frac{\Delta s_\xi^n}{\Delta \xi}\frac{\Delta s_{\eta i}^n}{\Delta \eta}, \tag{49}$$

where $\Delta s_\xi^n$ is given by (39) and

$$\Delta s_{\eta i}^n = \tfrac{1}{2}\sqrt{(r_{i+1}^n - r_{i-1}^n)^2 + (z_{i+1}^n - z_{i-1}^n)^2}, \tag{50}$$

is the grid spacing in the $\eta$ direction in the neighborhood of the node $(\xi_n, \eta_i)$.

With these estimates we can now generate predicted values for the nodes along the next coordinate line $\xi = \xi_{n+1}$ by integrating the system (44). Among the several numerical schemes for the integration of hyperbolic first-order systems, on the basis of the results of Ref. 26, we choose an implicit flux-vector splitting with artificial viscosity that leads to

$$\frac{\mathbf{W}_i^{n+1} - \mathbf{W}_i^n}{\Delta \xi} + \mathbf{C}_i^n \frac{\mathbf{W}_{i+1}^{n+1} - \mathbf{W}_{i-1}^{n+1}}{2\Delta \eta} = \mathbf{J}_i^n + \mu \frac{\mathbf{W}_{i+1}^{n+1} - 2\mathbf{W}_i^{n+1} + \mathbf{W}_{i-1}^{n+1}}{\Delta \eta^2}, \tag{51}$$

where $\mu$ is the artificial viscosity coefficient given by[27]

$$\mu = \tfrac{1}{2}\mathscr{A}\lambda. \tag{52}$$

Here, $\mathscr{A}$ is the grid aspect ratio defined by

$$\mathscr{A} = \frac{\Delta s_\xi^n}{\Delta s_{\eta i}^n}, \tag{53}$$

and $\pm\lambda$, with

$$\lambda = \frac{1}{(h_\eta^n)^2}\sqrt{(r_\xi^n r_\eta^n - z_\xi^n z_\eta^n)^2 + (r_\xi^n z_\eta^n + r_\eta^n z_\xi^n)^2}, \tag{54}$$

are the eigenvalues of the matrix **C**. The use of an artificial viscosity coefficient proportional to the local grid aspect ratio $\mathscr{A}$ mitigates the danger of grid crossing that is especially threatening when the bubble surface presents a strong concave curvature to the gas. This effect can be understood by noting that, in the present context, grid crossing is analogous to the formation of a shock wave[28] and can therefore be countered by a sufficiently strong viscosity. When the grid is about to cross, $\Delta s_\eta^{i,n}$ becomes very small, and the effective viscosity (52) correspondingly large. In spite of this fact, however, grid crossing would not be completely avoided near the end of the collapse, where the curvature of the surface is large. In this case, rather than generating the $(n+1)$-st coordinate line in one step, we take several substeps (up to 20).

After the predictor step, a corrector step is taken. The partial derivatives $r_\xi^n$, $z_\xi^n$ are updated by averaging with the previously estimated values (48). With these new estimates, the matrix **C** and the vector **J** are recalculated. For the latter quantity, in place of (45), we use

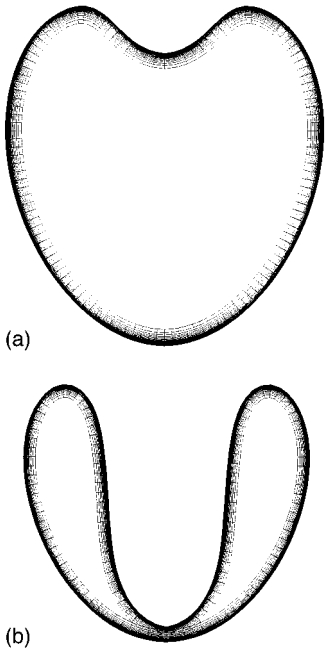


FIG. 2. Two examples of the grid generated by the technique of Sec. III B 1. These are the grids corresponding to the seventh and last frames of the collapse sequence shown in Fig. 6. Note the grid overlap near the jet tip in the second figure.

$$\mathbf{J} = \frac{J + \widetilde{J}}{(h_\eta^n)^2}(z_\eta^n, -r_\eta^n)^T, \tag{55}$$

where $\widetilde{J}$ is the value of $J$ used for the predictor step.

The numerical errors inherent in the procedure just described, and in particular the use of an artificial viscosity, have the adverse effect of deteriorating grid orthogonality. Our tests show that deviation from orthogonality is mostly small, of the order of 5°. Toward the end of the collapse, however, stronger deviations up to about 30° are encountered. Our[29] and others' (see, e.g., Ref. 30) experience indicates that, provided extreme non-orthogonality is avoided, orthogonality *per se* is not crucial. Therefore, rather than investing a considerable effort in the solution of the hyperbolic system, we find it more efficient to simply accept any residual non-orthogonality and use a non-orthogonal discretization of the differential equations.

Two examples of the grid generated by the technique just described are shown in Fig. 2. These are the grids corresponding to the seventh and the last frames of the collapse sequence shown in Fig. 6. Note in Fig. 2(b) the partial overlap of the grids near the axis of symmetry.

### 2. The inner boundary

The last grid line $\xi = 1$ constitutes the inner boundary for the domain in which the equations for the gas temperature $T$ and velocity potential $\Phi$ must be solved, and boundary conditions for these quantities are necessary.

For the temperature we simply stipulate

$$\mathbf{n}\cdot\nabla T = 0. \tag{56}$$

This condition is consistent with the assumption of negligible gradients in the bubble core, but allows the core temperature to adjust so as to conserve energy.

For $\Phi$, we find a Dirichlet boundary condition as follows. Since, according to (15), this field is harmonic, we can write for it a Green identity similar to (2)

$$\Phi(\mathbf{x})=\int_S\left[G(\mathbf{x},\mathbf{x}_s)\frac{\partial\Phi}{\partial n_s}-H(\mathbf{x},\mathbf{x}_s)\Phi(\mathbf{x}_s)\right]dS. \tag{57}$$

Here, as in (2), the integral is over the trace $S$ of the surface on a meridian plane, reflecting the fact that this relation is obtained from the Laplace equation in the three-dimensional domain. The normal derivative can be considered known from (20) so that the equation can be used to solve for the value of $\Phi$ on the bubble surface. After this step, Green's identity can be written again — this time for points on the $\xi=1$ grid line — to find the required boundary condition

$$\Phi(\mathbf{x})=2\int_S\left[G(\mathbf{x},\mathbf{x}_s)\frac{\partial\Phi}{\partial n_s}-H(\mathbf{x},\mathbf{x}_s)\Phi(\mathbf{x}_s)\right]dS. \tag{58}$$

The factor 2 arises from the difference in the solid angle under which the boundary is seen by an interior point as compared with a surface point. The arbitrary constant inherent in the solution of (57) is set to 0.

The previous relations are included in the iteration scheme described below, with the right-hand sides evaluated on the basis of the most recent values available.

Note that the use of the correct boundary condition for $\Phi$ gives a meaning to the solution for this field even in a region where the grid partially overlaps as in the example of Fig. 2(b). The equation is merely solved twice in the same region. Strictly speaking, this remark does not apply to the solution of the temperature field due to the zero-gradient condition (56). Nevertheless, as can be seen, e.g., from Fig. 11, the thermal boundary layer is so thin near the jet tip that the error is negligible.

### 3. Discretization of the gas equations

The Laplace (15) and energy (17) equations in the gas are discretized by finite differences. In principle one could use the relation (58) for $\Phi$ at every grid point, but this approach encounters near-singularities for the nodes near the boundary (see, e.g., Ref. 31) and is also fairly expensive in view of the large number of numerical quadratures required. We prefer therefore to use finite differences for the Laplace equation as well.

The Laplace equation in a general axi-symmetric, non-orthogonal curvilinear coordinate system can be written as

$$\frac{\partial}{\partial\xi}\left(r\frac{h_\eta^2}{J}\frac{\partial\Phi}{\partial\xi}-g\frac{\partial\Phi}{\partial\eta}\right)+\frac{\partial}{\partial\eta}\left(r\frac{h_\xi^2}{J}\frac{\partial\Phi}{\partial\eta}-g\frac{\partial\Phi}{\partial\xi}\right)=0, \tag{59}$$

where

$$g=r\frac{r_\xi r_\eta+z_\xi z_\eta}{J}. \tag{60}$$

We let

$$\xi_i=-1+i\Delta\xi,\quad 0\leqslant i\leqslant N_\xi,\quad \eta_j=-1+j\Delta\eta,$$
$$0\leqslant j\leqslant N_\eta, \tag{61}$$

and use central differences to find

$$\sum_{l,m=-1}^{1}c_{l,m}^{i,j}\Phi_{i+l,j+m}=0. \tag{62}$$

The coefficients of this difference equation are given by

$$c_{\pm1,0}^{i,j}=\frac{1}{\Delta\xi^2}\left(\frac{h_\eta^2 r}{J}\right)_{i,j+1/2}\mp\frac{1}{4\Delta\xi\Delta\eta}[g_{i\pm1/2,j}-g_{i,j-1/2}],$$
$$c_{0,\pm1}^{i,j}=\frac{1}{\Delta\eta^2}\left(\frac{h_\xi^2 r}{J}\right)_{i,j\pm1/2}\mp\frac{1}{4\Delta\xi\Delta\eta}[g_{i+1/2,j}-g_{i-1/2,j}],$$
$$c_{-1,\pm1}^{i,j}=\pm\frac{1}{4\Delta\xi\Delta\eta}[g_{i-1/2,j}+g_{i,j\pm1/2}], \tag{63}$$
$$c_{\pm1,1}^{i,j}=\mp\frac{1}{4\Delta\xi\Delta\eta}[g_{i+1/2,j}+g_{i,j\pm1/2}],$$
$$c_{0,0}^{i,j}=-c_{-1,0}^{i,j}-c_{0,-1}^{i,j}-c_{1,0}^{i,j}-c_{0,1}^{i,j}.$$

Half-step values are obtained by averaging.

The boundary conditions for $\Phi$ are specified by

$$\Phi_{0,j}=\Phi(-1,\eta_j),\quad \Phi_{N_\xi,j}=\Phi(1,\eta_j), \tag{64}$$
$$\Phi_{i,0}=\tfrac{1}{3}(4\Phi_{i,1}-\Phi_{i,2}),$$
$$\Phi_{i,N_\eta}=\tfrac{1}{3}(4\Phi_{i,N_\eta-1}-\Phi_{i,N_\eta-2}). \tag{65}$$

The last two relations express the vanishing of the normal gradient of $\Phi$ on the axis of symmetry and have been obtained by using the second-order accurate, one-sided derivative formula.

In axi-symmetric, non-orthogonal curvilinear coordinates moving with a velocity field $\mathbf{V}$, the energy equation (17) takes the form of

$$\rho_G C_p\left(\frac{\partial T}{\partial t}+\frac{u_\xi-V_\xi}{h_\xi}\frac{\partial T}{\partial\xi}+\frac{u_\eta-V_\xi}{h_\eta}\frac{\partial T}{\partial\eta}\right)$$
$$=\dot{p}+\frac{1}{Jr}\left[\frac{\partial}{\partial\xi}\left(k\frac{h_\eta^2 r}{J}\frac{\partial T}{\partial\xi}-kg\frac{\partial T}{\partial\eta}\right)+\frac{\partial}{\partial\eta}\right.$$
$$\left.\times\left(k\frac{h_\xi^2 r}{J}\frac{\partial T}{\partial\eta}-kg\frac{\partial T}{\partial\xi}\right)\right] \tag{66}$$

where, from (16),

$$u_\xi=-\frac{\dot{p}}{3\gamma p}\frac{h_\xi}{J}(rz_\eta-zr_\eta)+\frac{\gamma-1}{\gamma p}k\left(\frac{h_\eta h_\xi}{J}\right)^2$$
$$\times\left(\frac{1}{h_\xi}\frac{\partial T}{\partial\xi}-\frac{g_{12}}{h_\xi h_\eta}\frac{1}{h_\eta}\frac{\partial T}{\partial\eta}\right)+\left(\frac{h_\eta h_\xi}{J}\right)^2$$
$$\times\left(\frac{1}{h_\xi}\frac{\partial\Phi}{\partial\xi}-\frac{g_{12}}{h_\xi h_\eta}\frac{1}{h_\eta}\frac{\partial\Phi}{\partial\eta}\right), \tag{67}$$

$$u_\eta = -\frac{\dot{p}}{3\gamma p}\frac{h_\eta}{J}(-rz_\xi + zr_\xi) + \frac{\gamma-1}{\gamma p}k\left(\frac{h_\eta h_\xi}{J}\right)^2 \times\left(\frac{1}{h_\eta}\frac{\partial T}{\partial \eta} - \frac{g_{12}}{h_\xi h_\eta}\frac{1}{h_\xi}\frac{\partial T}{\partial \xi}\right) + \left(\frac{h_\eta h_\xi}{J}\right)^2 \times\left(\frac{1}{h_\eta}\frac{\partial \Phi}{\partial \eta} - \frac{g_{12}}{h_\xi h_\eta}\frac{1}{h_\xi}\frac{\partial \Phi}{\partial \xi}\right). \tag{68}$$

Here, $g_{12}$ is defined in (37) and the metric coefficient in the $\xi$ direction, $h_\xi$, is given by

$$h_\xi = (r_\xi^2 + z_\xi^2)^{1/2}. \tag{69}$$

The grid velocity $\mathbf{V}=(V_\xi, V_\eta)$ is calculated by dividing the difference between the new and old node positions by the time step $\Delta t$. Time integration is effected by using the trapezoidal rule for both the diffusion and convection terms. The space derivatives in the convection term are discretized using first-order upwinding. The resulting algebraic system has the form

$$\sum_{l,m=-1}^{1} C_{l,m} T_{i+l,j+m}^{n+1} = F_{i,j}^{n+1/2}, \tag{70}$$

where the $C_{l,m}$ are given by

$$C_{\pm 1,0} = \frac{1}{(Jr)_{i,j}\Delta\xi}\left\{\frac{1}{\Delta\xi}\left(\frac{h_\eta^2 rk}{J}\right)_{i\pm 1/2,j} \mp \frac{1}{4\Delta\eta}[(gk)_{i,j+1/2} - (gk)_{i,j-1/2}]\right\},$$

$$C_{0,\pm 1} = \frac{1}{(Jr)_{i,j}\Delta\eta}\left\{\frac{1}{\Delta\eta}\left(\frac{h_\xi^2 rk}{J}\right)_{i,j\pm 1/2} \mp \frac{1}{4\Delta\xi}[(gk)_{i+1/2,j} - (gk)_{i-1/2,j}]\right\},$$

$$C_{-1,\pm 1} = \pm\frac{1}{(Jr)_{i,j}}\frac{1}{4\Delta\xi\Delta\eta}[(gk)_{i-1/2,j} + (gk)_{i,j\pm 1/2}],$$

$$C_{1,\pm 1} = \mp\frac{1}{(Jr)_{i,j}}\frac{1}{4\Delta\xi\Delta\eta}[(gk)_{i+1/2,j} + (gk)_{i,j\pm 1/2}], \tag{71}$$

$$C_{0,0} = \frac{C_p\rho_G^{n+1/2}}{\Delta t} - C_{0,-1} - C_{-1,0} - C_{1,0} - C_{0,1}. \tag{72}$$

The only temperature dependence of the first four coefficients is through the gas thermal conductivity $k$. To evaluate this quantity we use the most recently available value of the temperature. We evaluate $\rho_G^{n+1/2}$ as $\frac{1}{2}(\rho_G^n + \rho_G^{n+1})$ with the value at time level $n+1$ calculated from the most recently updated value of $T$ using the equation of state (11). The right-hand side of (70) is given by

$$F_{i,j}^{n+1/2} = C_p(\rho_G)_{i,j}^{n+1/2}\frac{T_{i,j}^n}{\Delta t} + \dot{p}^{n+1/2} + \frac{1}{2}\left(\frac{1}{Jr}\left[\frac{\partial}{\partial\xi}\left(r\frac{h_\eta^2}{J}k\frac{\partial T}{\partial\xi} - gk\frac{\partial T}{\partial\eta}\right) + \frac{\partial}{\partial\eta}\left(r\frac{h_\xi^2}{J}k\frac{\partial T}{\partial\eta} - gk\frac{\partial T}{\partial\xi}\right)\right]\right)_{i,j}^n - C_p\rho_G^{n+1/2}\left(\frac{u_\xi - V_\xi}{h_\xi}\frac{\partial T}{\partial\xi} + \frac{u_\eta - V_\eta}{h_\eta}\frac{\partial T}{\partial\eta}\right)_{i,j}^{n+1/2}. \tag{73}$$

The half-time-step values are obtained by averaging as before.

The boundary conditions are similar to those on $\Phi$, Eq. (65)

$$T_{N_\xi,j}^{n+1} = \tfrac{1}{3}(4T_{N_\xi-1}^{n+1} - T_{N_\xi-2,j}^{n+1}), \quad T_{0,j}^{n+1} = T_\infty,$$
$$T_{i,0}^{n+1} = \tfrac{1}{3}(4T_{i,1}^{n+1} - T_{i,2}^{n+1}),$$
$$T_{i,N_\eta}^{n+1} = \tfrac{1}{3}(4T_{i,N_\eta-1}^{n+1} - T_{i,N_\eta-2}^{n+1}). \tag{74}$$

It is worth pointing out that, in spite of our use of a moving grid, the use of the convective derivative in the form (18) — in which the partial derivative is taken following the grid point — and the fact that the grid is structured, avoid the need to interpolate the temperature field onto the new grid at the beginning of each time step. This point is important as the interpolation procedure is subject to numerical diffusion artifacts.

#### 4. Iteration procedure

The field $\Phi$ depends on the gas temperature and pressure through its boundary condition (20), and it also appears in the energy equation through the non-linear convection terms. The gas velocity and temperature fields are therefore coupled and an iterative procedure is used for their determination. In the present time-dependent problem convergence is particularly rapid as values at the previous time step furnish excellent initial estimates for the various quantities.

The Laplace equation (59) for $\Phi$ is solved first by using the current estimates of $T$ and $\dot{p}$ in the boundary condition (20). In this way an updated estimate of the gas velocity field is generated and the energy equation (66) can be solved for $T$. For this step, the thermal conductivity is estimated from the most recently evaluated values of $T$.

At this point updated values for the surface heat flux and total heat transfer rate $\dot{Q}$ can be calculated to give an updated value for $\dot{p}$, which is then used to find a new estimate of $\Phi$, and so on until convergence is attained. Several convergence criteria were tried and it was found that monitoring the total heat flux across the bubble wall is sufficient.

In solving the Laplace equation (62), successive over-relaxation is used with the relaxation parameter ranging between 1.5 and 1.95, depending on the grid aspect ratio. Under-relaxation is used for the energy equation with a relaxation parameter of 0.8.

### C. Validation

The accuracy of the computational procedure has been tested first of all by carrying out the standard convergence and grid refinement studies.

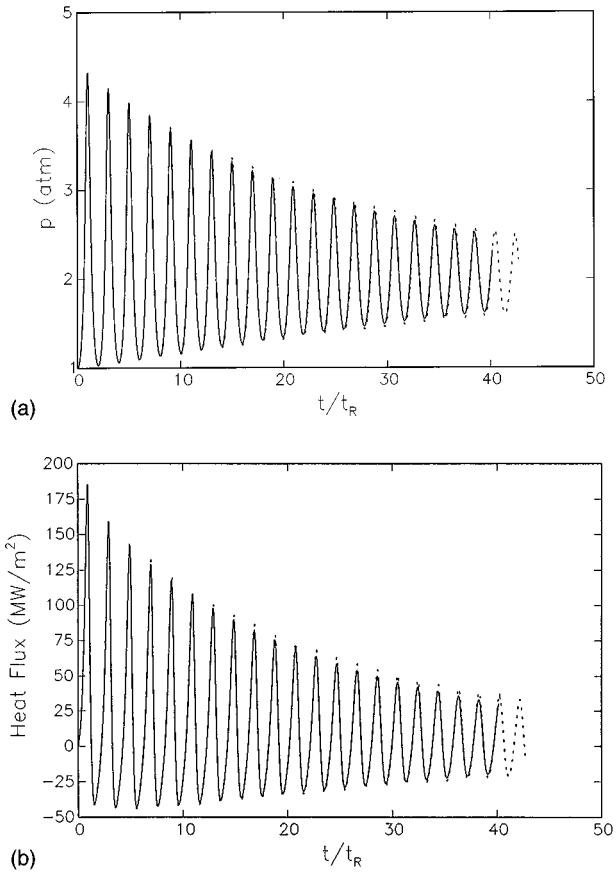


FIG. 3. Internal pressure, (a), and heat flux, (b), for a 1 mm radius air bubble initially in equilibrium at 1 atm, and subjected to a sudden overpressure of 1 atm. The results computed by the present method are shown by the solid line, while the dashed line gives the results given by the spherically symmetric model of Ref. 5. Time is in units of $t/t_R$, where $t_R$ is the Rayleigh collapse time defined in (41). With the parameter values of this example, $t_R$=110 $\mu$s.

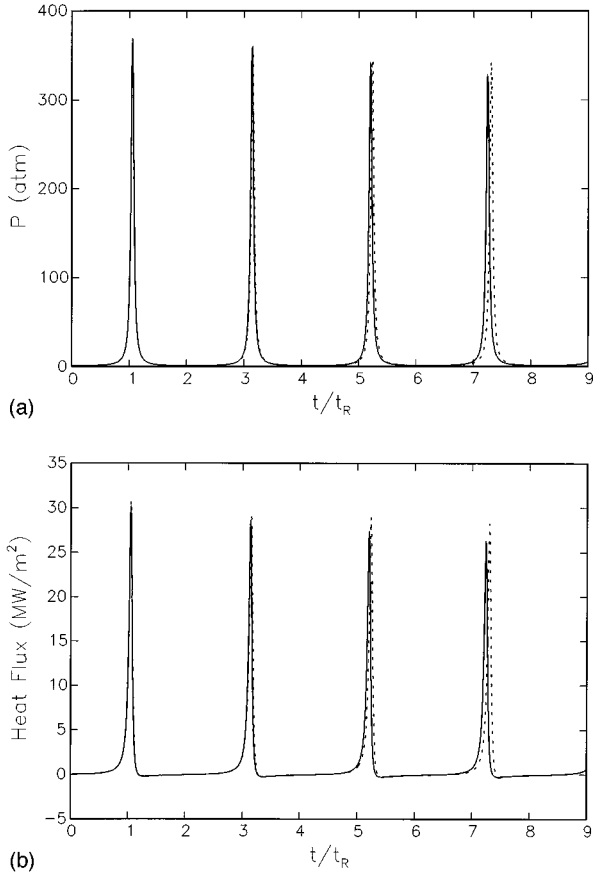


FIG. 4. Internal pressure, (a), and heat flux, (b), for a 1 mm radius air bubble initially in equilibrium at 1 atm, and subjected to a sudden overpressure of 10 atm. The results computed by the present method are shown by the solid line, while the dashed line gives the results of the spherically symmetric model of Ref. 5. Time is in units of $t/t_R$, where $t_R$ is the Rayleigh collapse time defined in (41). With the parameter values of this example, $t_R$=34.9 $\mu$s.

For a better validation, however, we have compared the results with those obtained by the method of Ref. 5 in which the spherically symmetric version of the mathematical model of Sec. II is solved. Since the numerical aspects of the two calculations are very different from each other, this comparison may be regarded as a significant test. A limitation of the comparison lies in the fact that, even in the absence of boundaries, the spherical shape is subject to well-known instabilities that are of course unaccounted for in the spherical model. Nevertheless, we have found that the instability is minor up to the time when the simulation was terminated. All the calculations have been carried out with $41\times65$ nodes.

Figure 3(a) shows the internal pressure of a bubble subjected to a suddenly applied overpressure $\Delta P=1$ atm as a function of the dimensionless time scaled by the Rayleigh collapse time $t_R$ given by Eq. (41) and equal to 110 $\mu$s. Initially the bubble has a radius of 1 mm and is in equilibrium under an ambient pressure of 1 atm. The solid line is the result of the present model and the dashed line that of the spherically-symmetric calculation. The response consists of a series of nonlinear damped oscillations. The maximum internal pressure reached at the end of the first collapse is approximately 4.3 atm. The heat fluxes into the liquid are compared in Fig. 3(b).

Figure 4 shows similar results for an overpressure of 10 atm. Here, $t_R$=34.9 $\mu$s and the maximum internal pressure exceeds 370 atm. The two formulations are in broad agreement, except that a phase difference gradually develops over time. This feature is not surprising upon comparison of two different free-oscillation calculations where small differences can accumulate and give rise to appreciable phase discrepancies at long times.

On the basis of these and several other tests of a similar nature that we have conducted, we are confident that the numerical method is reliable.

Below, the liquid temperature will be estimated by solving the heat conduction equation normal to the bubble surface with the computed surface heat flux and the neglect of convection. Since the spherical model contains convection, we can examine here the validity of this approximation. Figure 5 compares the surface temperatures estimated by pure conduction (solid line) and by including convection during the first collapse of Fig. 4. The differences are significant and they are due to the fact that the inward spherical motion

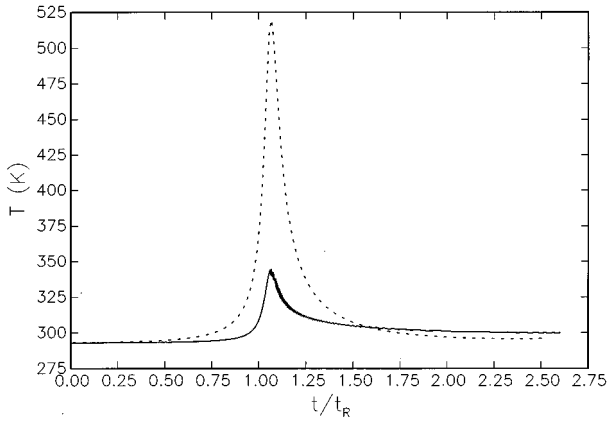


FIG. 5. Estimated liquid temperature without (solid line) and with convection effects in the liquid during the first collapse shown in Fig. 4.

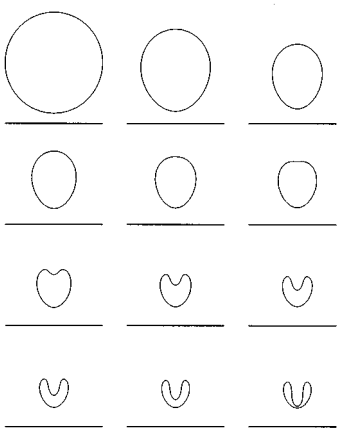

FIG. 6. Succesive shapes of a 1 mm radius bubble with center 1.2 mm away from a rigid wall after the application of an overpressure of 10 atm. The nondimensional times are $t/t_R=0$, 0.842, 1.037, 1.080, 1.106, 1.122, 1.151, 1.174, 1.184, 1.194, 1.203, and 1.219. The Rayleigh collapse time $t_R$ equals 34.9 $\mu$s.

stretches the thermal boundary layer thus decreasing the conductive heat loss from the surface.

One can get a handle on the difference between the two results with the following argument. Consider a thermal layer of thickness $\delta_1$ surrounding the surface of a sphere of radius $a_1 \gg \delta_1$. If the sphere shrinks to a radius $a_2$, the thermal layer thickness becomes, approximately, $\delta_2=(a_1/a_2)\delta_1$. As a rough approximation one can account for this effect by decreasing the thermal conductivity of the liquid. From the appearance of the second derivative in the diffusion equation, one deduces that the ''effective'' thermal conductivity should be reduced by $(a_1/a_2)^2$. From the well-known expression for the surface temperature of a semi-infinite solid subject to a surface heat flux $q(t)$ we have

$$T-T_\infty=\frac{1}{\sqrt{\pi k_L \rho_L C_{pL}}}\int_0^t d\tau \frac{q(\tau)}{\sqrt{t-\tau}}. \tag{75}$$

This relation shows that, for a given heat flux, the temperature increase varies inversely with the square root of the thermal conductivity, i.e., by the previous argument, proportionately to $a_1/a_2$. For the case of Figs. 4 and 5, with $a_1=a$ and $a_2$ equal to the computed minimum radius 0.24 $a$, we expect the ratio of the temperature increases obtained with and without convection to be approximately 4, in excellent agreement with the result shown in Fig. 5. We return to this estimate later.

## IV. RESULTS

We study the response of initially spherical air bubbles to two different pressure loadings, a sudden overpressure, and a Gaussian pressure profile. We consider bubbles with initial radii of 1 and 0.1 mm at different distances from a rigid plane wall. In all cases the equilibrium ambient pressure is $P_a=1$ atm and the undisturbed temperature 20 °C. The liquid is Liquid Gun Propellant 1845 with $\rho_L=1{,}452$ kg/m$^3$, thermal conductivity $k_L=0.15$ W/mK, and specific heat $C_{pL}=2{,}300$ J/kg K, but some results for water are also given.

For all the calculations that follow we used 65 nodes on the surface and 41 and 65 nodes in the $\xi$ and $\eta$ directions respectively. The time step is chosen adaptively in such a way that the increase of the maximum surface velocity, heat flux, and pressure always remains less than 0.1%.

### A. Sudden pressurization

A bubble with its center at a distance $b$ from a rigid plane wall and radius $a$ initially at equilibrium under a pressure $P_a=1$ atm is subjected at time 0+ to the pressure $p_\infty=P_a+\Delta P$. It is well known that in these conditions, as the collapse proceeds, a jet develops in the bubble directed toward the boundary.[7,8,10] The Rayleigh collapse time (41), that gives the correct time scale for this situation asymptotically for $\Delta P \gg P_a$, is used to nondimensionalize time.

As our reference case we take a 1 mm radius bubble whose center is 1.2 mm away from the wall so that $b/a=1.2$. The overpressure is $\Delta P=10$ atm which gives $t_R=34.9$ $\mu$s. Figure 6 shows a series of snapshots of the bubble at different stages of the compression. The time elapsed between successive images is not constant and ranges between 0.842 dimensionless units for the first pair and 0.016 for the last one. The calculation is interrupted shortly before the jet tip touches the opposing side of the surface. Figure 7 shows the velocity of the jet tip as a function of time during the collapse. It is seen that for most of the process this velocity is a few tens of m/s, with a maximum of the order of 300 m/s reached in the last few instants. These values are quite modest compared with the speed of sound in the liquid, which justifies the assumption of liquid incompressibility. As we show in Fig. 10, discussed later, the gas temperature toward the end of the collapse is about four times as large as the initial value, so that the speed of sound has doubled to over 600 m/s. Thus, while the jet Mach number with respect to the gas reaches a maximum value of about 0.5, which is not small, our assumption of a uniform gas pressure is likely to be inaccurate only over the last few percent of the collapse time and one would not expect this circumstance to induce order-of-magnitude errors in the results.

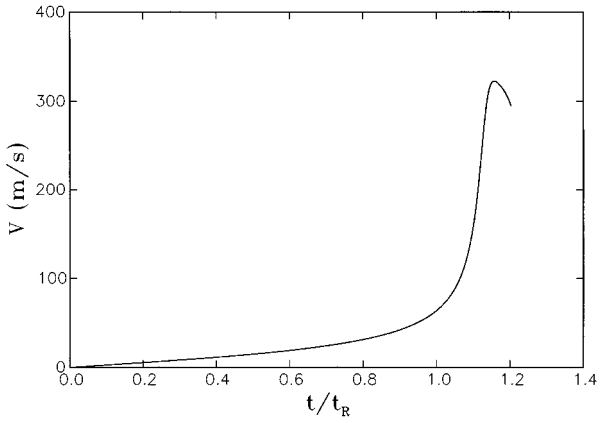


FIG. 7. Jet tip velocity as a function of time for the case of the previous figure.

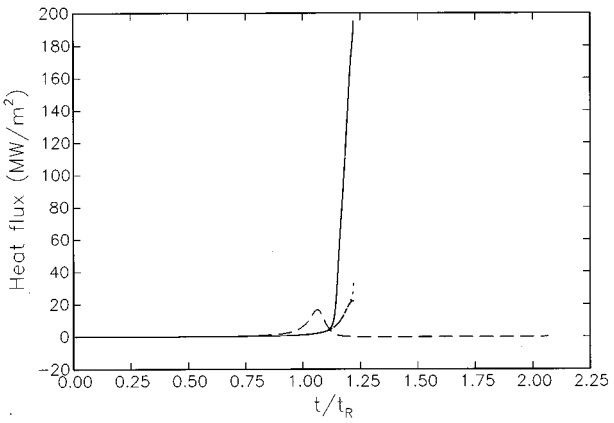


FIG. 9. Heat flux into the liquid at the ''north'' (solid) and ''south'' (dotted) poles of the bubble of Fig. 6 and at the midpoint of the surface, $\eta = 0$. The long-dash line shows the corresponding results for the spherical collapse of a 1 mm bubble.

The heat flux into the liquid along the bubble surface at different times is shown in Fig. 8 in which the abscissa is the coordinate $\eta$ ranging from $-1$ at the bubble's ''north pole'' (away from the wall) to 1 at the south pole (Fig. 1). Initially the curves are fairly flat, but when the jet starts developing the heat flux in the jet region becomes larger and larger, well exceeding 100 MW/m$^2$ in the last stages of the collapse. A different perspective on these results is provided by Fig. 9, where the dashed line gives the heat flux as a function of time for spherical collapse under the same conditions. The other three lines in the figure refer to the deforming bubble collapse, with the solid one corresponding to the north pole (jet), the dotted line to the south pole, and the remaining one to the point $\eta = 0$. The heat flux is seen to be nearly uniform over the surface of the bubble for most of the process. Toward the end, heat fluxes tend to be greater than for the spherical case, with the jet tip far exceeding all other points. Of course, comparisons at equal times between the spherical and non-spherical collapse are not meaningful due to wall-induced differences in the dynamics. Similar results for a 0.1 mm bubble collapsing at the same scaled distance $b/a$ from the wall, when plotted versus the appropriate scaled time, show the heat flux for the smaller bubble to be very close to $\sqrt{10}$ times that of the larger bubbles at all times. This reflects the fact pointed out at the end of section 3 that the boundary layer thickness scales as the square root of the characteristic time, which, in turn, is proportional to the radius.

As noted before, we use the computed heat flux to estimate the liquid temperature by solving the one-dimensional conduction equation in the direction normal to the interface. The results are shown in Fig. 10. Here, again the dashed line is for a 1 mm radius spherical collapse (including convection effects). The rapidly rising lines are the jet tip temperatures for 1 mm (solid) and 0.1 mm bubbles, and the other line (actually two lines superposed) are the liquid temperatures at the south pole and at the point $\eta=0$ for $a=1$ mm. While the jet tip reaches significantly higher temperatures than in the spherical case, the opposite is true for the other two points. In general, indeed, we find that heating is highly localized at the jet tip. The figure also shows that our procedure of solv-

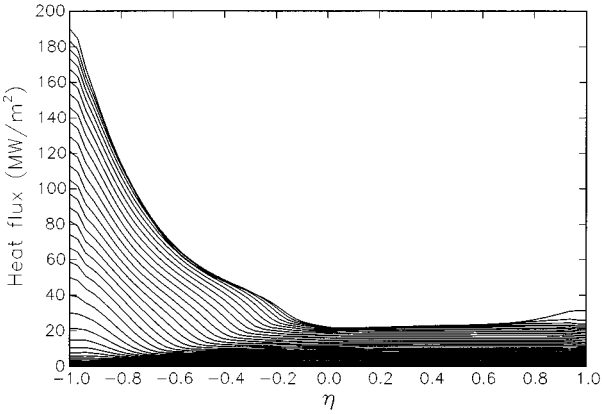


FIG. 8. Heat flux into the liquid along the bubble surface at different times for the collapse case of Fig. 6. The variable $\eta$ is the normalized arc length along the bubble surface with $\eta=-1$ corresponding to the jet tip on the axis of symmetry (see Fig. 1).

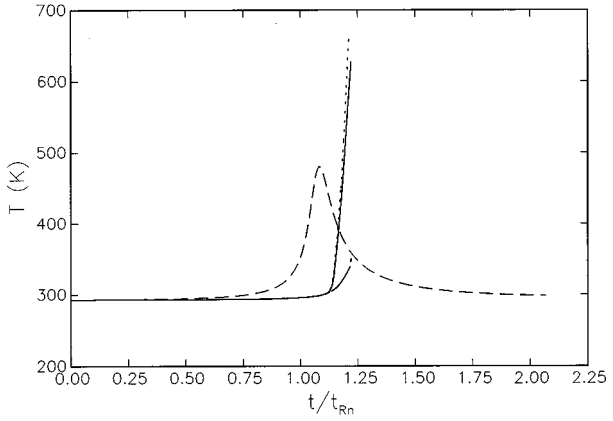


FIG. 10. Liquid temperatures at the ''north'' and ''south poles'' of the bubble of Fig. 6 and at the midpoint $\eta = 0$. The latter two curves are very nearly indistinguishable in the figure. The long-dash line shows the corresponding results for a spherical collapse under otherwise identical conditions of a 1 mm radius bubble far from the wall. Of the two rapidly rising lines, the solid one is for the north pole of a 1 mm radius bubble, and the other one for an initial radius of 0.1 mm.

ing the energy equation in the gas neglecting liquid heating is well justified for the major portion of the collapse process over most of the surface. The greatest error would occur at the jet tip, whose rapid heating at the very end would reduce the heat flux from the gas side. These results represent therefore an overestimate of the jet tip heating.

The curves in this figure come to an abrupt end when the calculation is interrupted just before the jet completely bridges the bubble. Presumably, just after this point, the hot tip liquid is quenched by mixing with the colder liquid surrounding the impact region. As the inward motion of the surface has not been arrested, however, some further compression of the gas may still occur, presumably followed by a fragmentation of the bubble. Since the temperature of the exposed liquid surface is still relatively low, as can be seen from Fig. 10 and as can also be inferred from the spherically symmetric results, one does not expect it to go much above 400 K during the residual compression phase. It should also be pointed out that, with other parameter values, we have found cases in which, just before the jet strikes the other side of the bubble, the velocity over the rest of the surface has already reversed. In these cases, one would not observe a residual gas compression following jet impact.

As discussed in Sec. III A, the procedure used to generate these results is inaccurate insofar as convection normal to the interface, that thickens the boundary layer, has been neglected. In the present case this effect is negligible in the jet region, which is nearly in rigid-body motion, and near the south pole, where motion is inhibited by the presence of the wall. The region most affected by the error is the lateral portion of the surface where the argument given in Sec. III A would give a temperature increase less than three times as large as the one calculated here. Even with this correction, the maximum temperature that one would expect is only slightly above 400 K.

According to the estimates quoted in the Introduction, ignition requires regions with linear dimensions of 0.1 to 10 $\mu$m that maintain a temperature above 700 K for 10 to 1000 $\mu$s. In the example considered here, 700 K are never reached. The time during which the tip temperature exceeds 500 K is about 3% of the Rayleigh collapse time, equal to 34.9 and 3.49 $\mu$s for $a=1$ and 0.1 mm, respectively. In view of the insufficient temperature, the brevity of the high-temperature duration, and the minute mass of hot liquid, it is doubtful that ignition could be caused by the jet. Ignition due to the residual gas compression also appears to be an unlikely event in view of the previous estimates.

The gas temperature along the axis of symmetry (normal to the wall) is shown in Fig. 11 at different times. The computed portions of the curves (corresponding to the resolved thermal layer) are shown by solid thin lines. The dashed straight lines have been interpolated for clarity. The solid heavy lines denote the adiabatic temperature based on the instantaneous bubble volume. The gas is very nearly adiabatic initially, but the temperature ends up somewhat lagging the adiabatic law due to the heat loss through the bubble surface. This figure also shows that the thermal boundary layer is adequately resolved in the calculation.

It is also of interest to compare the relative effect of heat

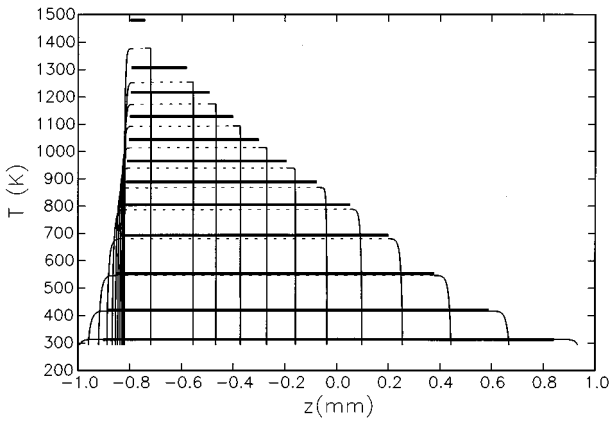


FIG. 11. Gas temperature along the axis of symmetry at different times for the collapse of Fig. 6. The computed portions of the curves (corresponding to the resolved thermal layer) are shown by the thin solid lines. The dashed lines have been interpolated for clarity. The thick solid lines are the adiabatic temperatures calculated from the instantaneous volume.

transfer and compression in determining the bubble internal pressure. These are the two terms in the right-hand side of the pressure equation (21), and are shown in Fig. 12 for a bubble radius of 100 $\mu$m. The solid line is the total $\dot{p}$, the dashed line the heat flux contribution $-(\gamma-1)Q/V$, and the dotted line the adiabatic compression contribution $\gamma p\dot{V}/V$. For this case heat transfer contributes less than 3% to the pressure variation over most of the collapse and would have an even smaller effect for a 1 mm bubble. If the process were followed over the course of many oscillations, however, the situation would of course be different as the thermal layer would grow to fill the whole bubble.

We have done a similar calculation with the physical properties of water. We have found virtually no differences in the bubble shape and the time derivative of the internal pressure provided everything is referred to the nondimensional time $t/t_R$, with $t_R$ accounting for the density difference between the two fluids. This scaling fails only at the

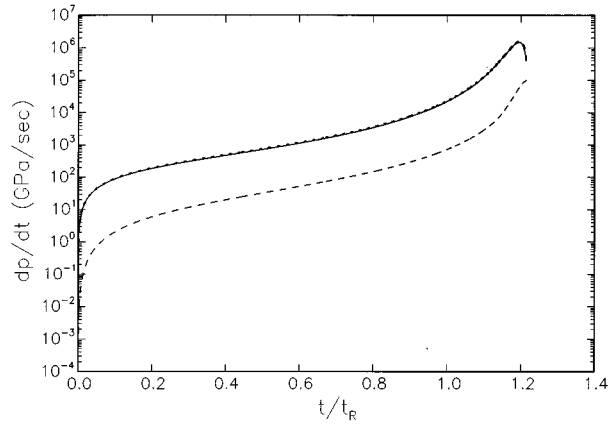


FIG. 12. The solid line is the time derivative of the bubble internal pressure $\dot{p}$ as given by (21) for the collapse process of Fig. 6 but with an initial bubble radius of 100 $\mu$m. The dashed and dotted lines are, respectively, the contribution of the heat transfer and adiabatic heating terms in the right-hand side of Eq. (21).

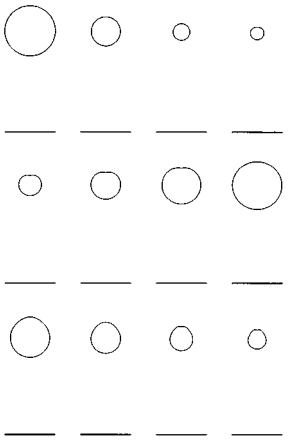

FIG. 13. Succesive shapes of a 1 mm radius bubble with center 4 mm away from a rigid wall after the application of an overpressure of 10 atm. The nondimensional times are $t/t_R = 0$, 0.9199, 1.055, 1.078, 1.115, 1.148, 1.341, 1.728, 2.552, 2.978, 3.124, and 3.175. The Rayleigh collapse time $t_R$ defined in (41) equals 34.9 $\mu$s.

very end of the collapse where slight differences in the heat fluxes into the jet tip start appearing. The biggest difference between the two cases is in the jet tip temperature due to the nearly quadruple thermal conductivity and double specific heat of water. We find that the maximum temperature reached by the jet tip in water is about 400 K, to be compared with over 600 K for the monopropellant case. The difference between the two results is in excellent agreement with the scaling that can be deduced from (75) written in terms of the scaled time $t/t_R$. Of course, since no evaporation is allowed in our model, these results are only indicative of the relative trends between the two liquids.

We can now consider a few other cases. Figure 13 is similar to Fig. 6, except that here the bubble center is at 4 mm from the solid wall, $b/a = 4$. In this case the influence of the wall is not large enough to cause pronounced jetting and one only observes relatively mild capillary waves. It is therefore evident that there is a critical bubble-wall separation

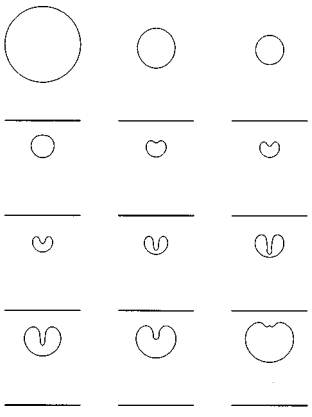

FIG. 14. Succesive shapes of a 1 mm radius bubble with center 2 mm away from a rigid wall after the application of an overpressure of 10 atm. The nondimensional times are $t/t_R = 0$, 1.012, 1.084, 1.115, 1.140, 1.150, 1.159, 1.170, 1.177, 1.185, 1.215, and 1.296. The Rayleigh collapse time $t_R$ defined in (41) equals 34.9 $\mu$s.

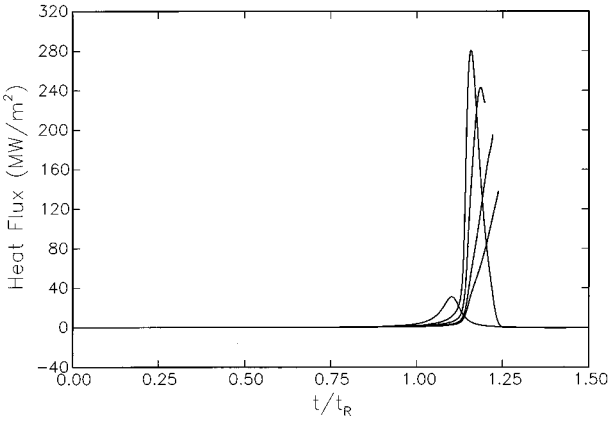


FIG. 15. Heat flux at the jet tip as a function of scaled time for different values of the wall separation $b$ and 1 mm radius bubbles. From the left, the lines correspond to $b/a = 4$, 2, 1.5, 1.2, 1.05.

such that the jet just touches the other side of the cavity at the moment the bubble starts rebounding. For the present parameter values, this critical distance is close to 2 mm, which is the case shown in Fig. 14.

The heat flux at the jet tip is shown as a function of time for different values of $b$ and 1 mm radius bubbles in Fig. 15. If the bubble starts rebounding before the jet pierces it (at which time the calculation is interrupted), the heat flux exhibits a maximum at the moment of maximum compression. These are the first three lines (counting from the left), corresponding to $b/a = 4$, 2, and 1.5, respectively. As the initial bubble center is taken closer and closer to the wall, the jet develops earlier and earlier and therefore it also strikes the other side before the gas has undergone its maximum possible compression. The resulting heating is therefore smaller. The values of the jet tip temperatures corresponding to these results are shown in Fig. 16. Corresponding results for a 0.1 mm radius bubble are shown in Figs. 17 and 18.

It may be noted that, in all these last results in which the jet rebounds, our assumption of negligible vorticity in the gas [see the text following Eq. (14)] is likely to be violated. Due to the limited effect of heat transfer on the gas pressure,

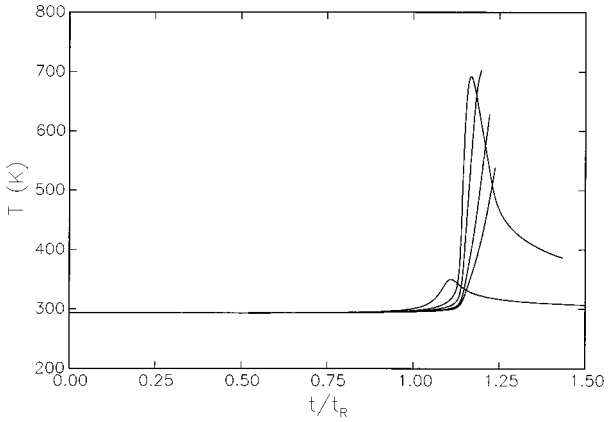


FIG. 16. Jet tip temperature as a function of scaled time for the cases of the preceding figure.

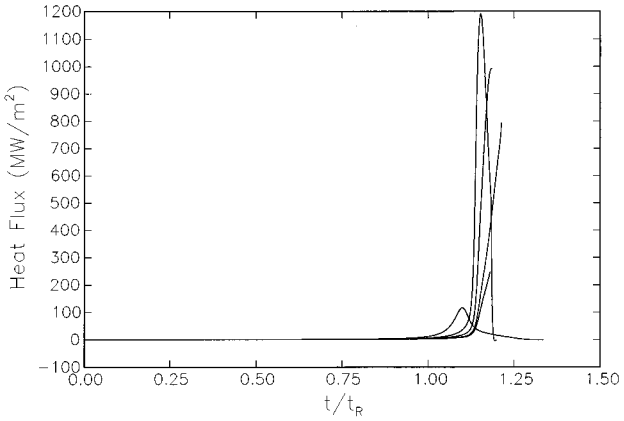


FIG. 17. Heat flux at the jet tip as a function of scaled time for different values of the wall separation $b$ and 0.1 mm radius bubbles. From the left, the lines correspond to $b/a = 4, 2, 1.5, 1.2, 1.05$.

shown in Fig. 12, one does not expect the dynamics to be affected by this circumstance. A limited effect on the portions of the curves of Figs. 15 to 18 following the maximum cannot, however, be ruled out.

### B. Gaussian pressure loading

For the Gaussian pressure loading we use the following pressure profile:

$$p_\infty = P_a + \Delta P \exp\left[-\frac{(t_*-5)^2}{\tau_*^2}\right], \tag{76}$$

again with $P_a=1$ atm, $a=1$ mm, $b=1.2$ mm, $\Delta P=10$ atm and $t_* = t/t_c$. The characteristic time $t_c$ is again taken as the Rayleigh time (41) and, with the previous parameter values, equals 34.9 $\mu$s.

Figure 19 is the heat flux into the jet tip as a function of time for a series of values of the parameter $\tau_*$ ranging, from left to right, from 2.8 to 0.3. The corresponding jet tip temperatures are shown in Fig. 20. As the value of $\tau_*$ is decreased from 2.8, at first the collapse occurs faster and the heat flux and temperature become gradually higher. For $1.6 \geqslant \tau_* \geqslant 0.5$ the violence of the motion causes the jet to

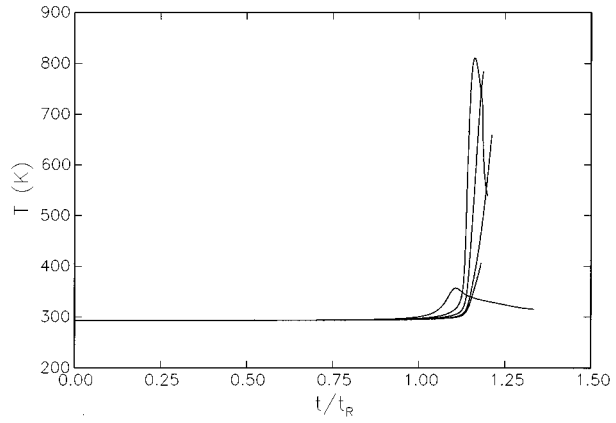


FIG. 18. Jet tip temperature as a function of scaled time for the cases of the preceding figure.

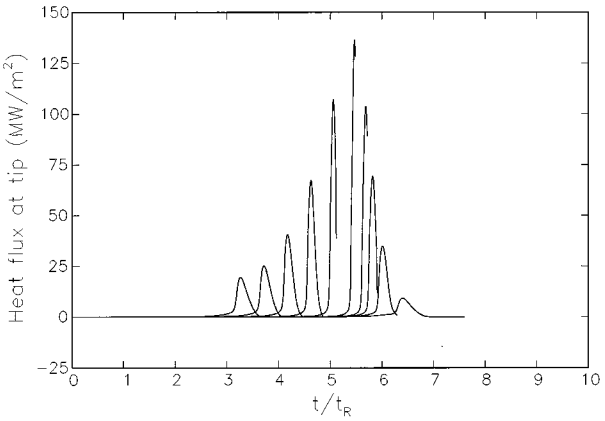


FIG. 19. Heat flux into the jet tip as a function of time for the Gaussian loading case of Eq. (76). The initial bubble radius is 1 mm and the initial distance from the wall 1.2 mm. The curves correspond to different values of the time scale $\tau$ of the applied overpressure. From the left, $\tau_* = 2.8, 2.4, 2, 1.6, 1.2, 0.8, 0.6, 0.5, 0.4, 0.3$.

pierce the bubble and the calculation must be stopped at the moment opposite sides meet. For still smaller value of $\tau_*$, the pressure change is too rapid to have a big effect on the bubble and the phenomenon is correspondingly reduced in intensity.

These results clearly display the effect of ''tuning'' the pulse's time scale to the bubble collapse time. This factor should be carefully taken into account when planning an experiment. In too small a tank with an explosive-produced loading of the bubble, the high pressure might last too little to achieve a significant compression.

The interpretation of these results is subject to the same note of caution appended at the end of the last subsection as to the effect of the neglect of the vorticity field in the gas.

## V. CONCLUSIONS

We have studied the thermal processes occurring in the gas contained in a bubble collapsing non-spherically in the neighborhood of a rigid wall. We have found that the dynamics of the bubble is not strongly affected by thermal effects for the size range considered here (0.1 to 1 mm), although

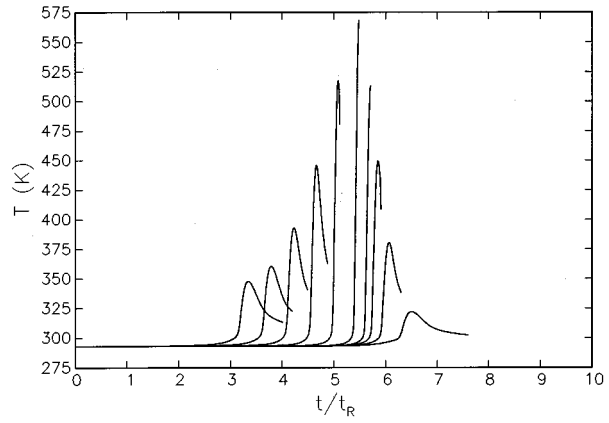


FIG. 20. Jet tip temperatures for the Gaussian loading cases of the previous figure. From the left, $\tau_* = 2.8, 2.4, 2, 1.6, 1.2, 0.8, 0.6, 0.5, 0.4, 0.3$.

the liquid in the tip of the wall-directed jet that forms under these conditions does heat up substantially more than in the case of spherical collapse. While the temperatures reached can be high, their duration is very brief, typically a few percent of the Rayleigh collapse time defined in (41), or a few microseconds. At the relatively low impact velocities (less than 400 m/s) of the cases considered here one expects that, when the jet strikes the other side of the bubble, it will be immediately quenched by mixing with much colder liquid.

The results discussed in the previous section have been obtained with the bubble subjected to a maximum overpressure $\Delta P$ of 10 atm. For higher values of $\Delta P$, the validity of some of the assumptions of the model (notably liquid incompressibility, spatial uniformity of the gas pressure, and lack of phase change) become questionable. Nevertheless, the results should be indicative of the orders of magnitude. With $\Delta P = 100$ atm the gas temperature reaches nearly 3500 K, but still the liquid temperature exceeds 500 K only for less than 0.2 $\mu$s.

A spherical bubble subject to a sudden overpressure differs in two major regards from the deforming bubble considered here. In the first place, with spherical symmetry, there must be an instant at which the kinetic energy vanishes. For a deformed bubble straddled by a jet the situation is different as some kinetic energy is stored in the vortex formed when the jet strikes the other side of the bubble.[11,32] As a consequence, the pressures (and therefore temperatures) found in the spherical collapse are higher than for a deforming bubble. Second, a spherical bubble executes a series of damped non-linear oscillations during which heat from the gas has ample time to diffuse to the surface and, on the average, heat up the liquid. This process cannot take place if the bubble breaks up. If a spherical bubble is subjected to higher and higher overpressures, the liquid on its surface will get hotter and hotter due to a combination of the two factors just described. For a deforming bubble, on the other hand, one has higher gas temperatures but the collapse and subsequent break up are so fast that the liquid has even less time to heat up. These considerations lead one to expect that liquid propellant ignition due gas heating in the course of bubble collapse is an unlikely event, at least for the parameter range investigated here.

Unfortunately, no data exist with which to make a direct quantitative comparison of our simulations. The majority of experiments have been conducted with cylindrical, rather than spherical, bubbles.[3,32,33] The dynamics in the two geometries can be expected to be significantly different. Two studies involved nearly spherical cavities,[4,34] but the results reported are mainly descriptive and cannot be compared with the present ones. In addition, in all these experiments, the bubble collapse was initiated by shock waves with strength of the order of several kbars, which represents another significant difference with the present model. In general, these studies have shown that ignition of liquid explosive due to gas bubble collapse is not a very reproducible phenomenon. As a matter of fact, Prof. Field opines (private communication) that contamination of the material probably played a major role in the observed events.

In the cases in which ignition occurred, it seemed to initiate at the point at which the jet hit the other side of the cavity.[3] The observed jet velocities were of the order of km/s, a situation far beyond the limits of validity of our study. Nevertheless, our results do indicate a strong heating of the jet tip and it is conceivable that this process sensitizes the tip liquid so that the compressive and viscoplastic heating occurring at the impact are sufficient for ignition. Light flashes indicative of reaction were also observed emanating from the gas surrounding the jet.[3,32,35,36] These can be imputed to adiabatic heating, which is a good approximation to the actual gas temperature as shown in Fig. 11.

The main difficulty in the present calculation resides in the extreme thinness of the thermal boundary layer in the gas, that requires a correspondingly fine spatial resolution. We have been able to obtain computationally efficient and accurate results by focusing on the region near the bubble surface with a hyperbolically generated boundary-fitted grid, realizing that the temperature in the bubble core would remain substantially uniform over the time intervals considered here. For this reason, our calculation is expected to be more accurate than the very similar one recently carried out by Takahira *et al.*[12] where a relatively coarse finite-element discretization of the entire bubble volume was used. Furthermore, contrary to that formulation, we have reduced the problem for the velocity potential in the gas to a Laplace, rather than Poisson, equation by identifying a particular integral of the non-homogeneous equation. This is another factor that greatly increases the efficiency of the computation.

## ACKNOWLEDGMENTS

We wish to thank Dr. Neil Bourne of the Cavendish Laboratory, Cambridge, U.K. for several helpful comments. He has also kindly made available to us his unpublished results on shock-induced spherical bubble collapse in LGP mentioned in the paper. Our sincere thanks also go to Dr. Hasan Oğuz who wrote the boundary integral code used to solve for the liquid motion and was generous with time and advice. The study has been supported by ARO under Grant No. DAAL04-93-G-0409 and by the Office of Naval Research.

[1] J.D. Knapton, N.A. Messina, and M. Tarczynski ''Some unsolved problems on ignition mechanisms in hydroxylammonium nitrate based liquid propellants,'' in *29th JANNAF Combustion Subcommittee Meeting* (Chemical Propulsion Information Agency, October, 1992).
[2] J.E. Field, ''Hot spot ignition mechanisms for explosives,'' Acc. Chem. Res. **25**, 489 (1992).
[3] N.K. Bourne and J.E. Field, ''Bubble collapse and the initiation of explosion,'' Proc. R. Soc. London, Ser. A **435**, 423 (1991).
[4] N.K. Bourne and S.M. Walley, ''Impact ignition of liquid propellants,'' Technical report, Physics & Chemistry of Solids, Cavendish Laboratory, University of Cambridge, 1993.
[5] V. Kamath and A. Prosperetti, ''Numerical integration methods in gas-bubble dynamics,'' J. Acoust. Soc. Am. **85**, 1538 (1989).
[6] V. Kamath, A. Prosperetti, and F. Egolfopoulos, ''A theoretical study of sonoluminescence,'' J. Acoust. Soc. Am. **93**, 248 (1993).
[7] M.S. Plesset and R.B. Chapman, ''Collapse of an initially spherical vapour cavity in the neighbourhood of a solid boundary,'' J. Fluid Mech. **47**, 283 (1971).
[8] W. Lauterborn and H. Bolle, ''Experimental investigations of cavitation-bubble collapse in the neighborhood of a solid boundary,'' J. Fluid Mech. **72**, 391 (1975).

[9]J.R. Blake and D.C. Gibson, ''Cavitation bubbles near boundaries,'' Ann. Rev. Fluid Mech. **19**, 99 (1987).
[10]W. Lauterborn and A. Vogel, ''Modern optical techniques in fluid mechanics,'' Annu. Rev. Fluid Mech. **16**, 223 (1984).
[11]T.B. Benjamin and A.T. Ellis, ''The collapse of cavitation bubbles and the pressures thereby produced against solid boundaries,'' Philos. Trans. R. Soc. London A **260**, 221 (1966).
[12]H. Takahira, H. Miyamoto, and T. Akamatsu, ''Numerical investigation of the thermal effects of the internal gas on the collapse and rebound of non-spherical bubbles,'' in *1995 Cavitation and Multiphase Flow Forum - FED Vol. 210*, edited by J. Katz and Y. Matsumoto (ASME, New York, 1995), pp. 173–179.
[13]R.I. Nigmatulin and N.S. Khabeev, ''Heat exchange between a gas bubble and a liquid,'' Fluid Dyn. **9**, 759 (1974).
[14]A. Prosperetti, L.A. Crum, and K.W. Commander, ''Nonlinear bubble dynamics,'' J. Acoust. Soc. Am. **83**, 502 (1988).
[15]M.A. Jaswon and G.T. Symm, *Integral Equation Methods in Potential Theory and Elastostatics* (Academic, New York, 1977).
[16]L. Guerri, G. Lucca, and A. Prosperetti, ''A numerical method for the dynamics of non-spherical cavitation bubbles,'' in *Proceedings of the Second International Colloquium on Drops and Bubbles*, edited by D.H. Le Croissette (Jet Propulsion Laboratory, Pasadena, 1982).
[17]J.R. Blake, B.B. Taib, and G. Doherty, ''Transient cavities near boundaries. Part I. Rigid boundary,'' J. Fluid Mech. **170**, 479 (1986).
[18]C. Pozrikidis, *Boundary Integral and Singularity Methods for Linearized Viscous Flow* (Cambridge University, Cambridge, 1991).
[19]A. Prosperetti, ''The thermal behaviour of oscillating gas bubbles,'' J. Fluid Mech. **222** 587 (1991).
[20]M.S. Plesset and A. Prosperetti, ''Bubble dynamics and cavitation,'' Annu. Rev. Fluid Mech. **9**, 145 (1977).
[21]H.P. Greenspan and A. Nadim, ''On sonoluminescence of an oscillating gas bubble,'' Phys. Fluids A **5**, 1065 (1993).
[22]H.N. Oguz and A. Prosperetti, ''Bubble entrainment by the impact of drops on liquid surfaces,'' J. Fluid Mech. **219**, 143 (1990).
[23]W.H. Press, W.T. Vetterling, S.A. Teukolsky, and B.P. Flannery, *Numerical Recipes in FORTRAN*, 2nd edition (Cambridge University, Cambridge, 1992).
[24]A.V. Oppenheim, *Digital Signal Processing*, 2nd edition (Prentice Hall, Englewood Cliffs, 1975).
[25]C. Canuto, M.Y. Hussaini, A. Quarteroni, and T.A. Zang, *Spectral Methods in Fluid Dynamics* (Springer, Berlin, 1988).
[26]C.H. Tai, S.L. Yin, and C.J. Soong, ''A novel hyperbolic grid generation procedure with inherent adaptive dissipation,'' J. Comput. Phys. **116**, 173 (1995).
[27]P.L. Roe, ''Characteristic-based schemes for the euler equations,'' Annu. Rev. Fluid Mech. **18**, 337 (1986).
[28]H.A. Dwyer, ''A geometric interpretation of hyperbolic grid generation,'' Comput. Fluids **23**, 737 (1994).
[29]H. Huang and A. Prosperetti, ''Effect of grid orthogonality on the solution accuracy of the two-dimensional convection-diffusion equation,'' Numerical Heat Transfer B **26**, 1 (1994).
[30]D. Lee and Y.M. Tsuei, ''A formula for the estimation of truncation errors of convection terms in a curvilinear coordinate system,'' J. Comput. Phys. **98**, 90 (1992).
[31]S. Vijayakumar and D.E. Cormack, ''A new concept in near-singular integral evaluation: The continuation approach,'' SIAM J. Appl. Math. **49**, 1285 (1989).
[32]N.K. Bourne and J.E. Field, ''Shock-induced collapse of single cavities in liquids,'' J. Fluid Mech. **244**, 225 (1992).
[33]N.K. Bourne and J.E. Field, ''Cavity collapse in a liquid with solid particles,'' J. Fluid Mech. **25**, 149 (1994).
[34]G.D. Coley and J.E. Field, ''The role of cavities in the initiation and growth of explosion in liquids,'' Proc. R. Soc. London **335**, 67 (1973).
[35]J.P. Dear, J.E. Field, and A.J. Walton, ''Gas compression and jet formation in cavities collapsed by a shock wave,'' Nature **332**, 505 (1988).
[36]J.E. Field, ''Experimental studies of bubble collapse,'' in *Bubble Dynamics and Interface Phenomena*, edited by J.R. Blake, J.M. Boulton-Stone, and N.H. Thomas (Kluwer, Dordrecht, 1994).